Evidence for parity dependence in the neutron-^{40}Ar optical model potential

C. H. Johnson*
Oak Ridge National Laboratory, Oak Ridge, Tennessee 37831

R. F. Carlton
Middle Tennessee State University, Murfreesboro, Tennessee 37132

R. R. Winters
Denison University, Granville, Ohio 43023

(Received 27 August 1990)

The neutron dispersive optical model potential that was developed previously from an analysis of extensive data on the neutron-^{40}Ca system is adapted to the neutron-^{40}Ar system by adjusting the central depth of the local equivalent of the Hartree-Fock-type potential. The n-^{40}Ar data for this adjustment are the total cross section for $11 < E < 40$ MeV and the centroid energy for the observed single-particle and single-hole states of the valence shells. The resulting potential for n-^{40}Ar yields good predictions for the particle-hole gap for the valence shells and for the energy-averaged s-wave and p-wave scattering functions in the resonance region. However, it gives a poor prediction for the total cross section from 2 to 11 MeV. A similar discrepancy was observed earlier for ^{40}Ca. A parity dependence in the surface imaginary potential is suggested from a more careful examination of the s-wave and p-wave scattering functions for ^{40}Ar; that parity dependence gives a good prediction of the total cross section for 2 to 11 MeV.

I. INTRODUCTION

It has been known for many years that the phenomenological neutron optical model potential (OMP) exhibits a dichotomy between the low-energy region of approximately $0 < E < 10$ MeV and higher energies. In particular, models that were parametrized to fit neutron scattering and total cross sections for energies above 5–10 MeV usually predicted too high total cross sections at lower energies [1,2]. Also, there was evidence [3] from the s-wave and p-wave neutron strength functions deduced from resonance scattering that the diffuseness of the surface imaginary potential approaches a delta function at zero energy. Further evidence of anomalous behavior comes from a recent series of measurements and analyses [2,4–6] of differential cross sections for $E < 10$ MeV for targets of ^{51}V, ^{59}Co, ^{89}Y, and ^{209}Bi. These analyses show that the radius of the real potential increases with decreasing energy, the surface imaginary diffuseness decreases and, in some cases, the imaginary radius increases. Similar results were found [7] for scattering from ^{208}Pb.

Developments of the past few years, initiated largely by Mahaux and Ngô [8], have led to the present consensus that the phenomenological OMP should include real dispersive components which are connected to the imaginary potential by the dispersion relation. These components provide for a unified description for both the OMP at positive energies and the shell model at negative energies because they include the effect of the coupling of the single-particle degree of freedom to low-lying core excitations. The consequences are profound. The dispersion relation leads not only to good descriptions of data for a broad range of positive and negative energies but also to predictions of quantities such as spectroscopic factors, occupation numbers, and spectral functions of the bound particle and hole states [9].

One consequence for the neutron dispersive OMP is that a maximum is predicted near zero energy for the effective radius of the real part of the mean field. That is consistent with the above empirical observation that the radius for the real part for the conventional OMP increases at low energies. Consequently, it was reasonable to expect [1] that the addition of the dispersive terms would remove the dichotomy in total cross sections. Indeed, an analysis [1] of the total cross section for ^{40}Ca for $0 < E < 10$ MeV led to the conclusion that the anomaly is removed; however, analyses [10,11] of more extensive data showed that the predicted total cross section is still to high for $0 < E < 10$ MeV. The integral nature of the dispersion relation implies that one must utilize as much data as possible for a wide range of positive and negative energies. For the n-^{40}Ca analysis [10,11], which is of particular interest here, the data included (i) the total cross section for neutron energies from 1 to 80 MeV, (ii) differential cross sections at 14 neutron energies from 5 to 40 MeV, (iii) analyzing powers for 5 energies from 10 to 17 MeV, and (iv) single-particle and single-hole bound-state energies not only for the valence orbits but also for deeply bound states down to -66 MeV.

There are presently two methods [12,13] for deducing a dispersive OMP from an analysis of such extensive data sets; the methods are quite different but lead to essentially the same results. For one method [12], called DOMA (dispersive optical model analysis), the dispersion relation is included for the primary fitting of experimental data.

This method has been applied [10,12,14–16] for n-^{40}Ca, p-^{40}Ca, n-^{90}Zr, n-^{208}Pb, and n-^{209}Bi. The other method is the moment approach for which one fits the data at each energy using a conventional model, without the dispersive terms, and subsequently deduces the dispersive model from the radial moments of the resulting potentials. The most advanced version is the variational moment approach [13] or VMA. It has been applied to the n-^{208}Pb and p-^{208}Pb systems [13,9,17] and to the n-^{40}Ca and p-^{40}Ca systems [11]. Less developed moment methods were used [2,5,6,18] for n-^{51}V, n-^{59}Co, n-^{89}Y, and n-^{209}Bi; for these cases, differential cross sections were available only for $E<10$ MeV.

The various DOMA and VMA have used "fixed geometry;" i.e., all geometric shape parameters are assumed to be independent of energy. It is remarkable that such a simple model, with the dispersive terms included, provides such an accurate description of the nucleon-nucleus mean field for such broad regions of both positive and negative energies [9–17]; nevertheless, several of the analyses suggest that further refinements are needed for $0<E<10$ MeV. As stated above, the n-^{40}Ca dispersive OMP [10,11] predicts neutron total cross sections for $0<E<10$ MeV which are systematically larger than the observed energy-averaged values. Calculations in Ref. [10] suggested that this discrepancy might be removed by making the shape of the surface imaginary potential energy dependent in a manner similar to that cited above for conventional OMP analysis; however, those calculations did not include the effect of the intricate shape [19] of the surface dispersive term that results from the energy-dependent shape of the imaginary potential. An analysis which did include the effects of the intricate shapes for the n-^{208}Pb system showed [19] that there is probably a small decrease at low energies in the diffuseness of the surface imaginary potential. These calculations showed, however, that a low-energy increase in the radius is not acceptable because that would lead to misfits to the bound single-particle energies.

A possible alternative refinement [19] for the low-energy region is a model which retains fixed geometry but includes an l dependence in the surface imaginary strength. There is presently little theoretical guidance for a detailed l dependence at low energies. Some guidance can be found in the positions of the surface radial nodes for each partial wave [19,20]. A recent suggestion [11] is that the imaginary strengths for those l values associated with the unfilled bound orbits should vanish below the corresponding single-particle energies. Both of these guiding criteria suggest that the l dependence is essentially a parity dependence. Empirically, only a simple l dependence can be justified by the limited information contained in the total and differential cross sections. For example, in a study [12,19,20] of n-^{208}Pb, the l values were separated into only two groups with different surface imaginary depths to give the best fit to the data.

There is one experimental procedure that gives specific information on the OMP scattering functions for the first few partial waves at low energies. It is to measure the low-energy neutron total cross sections with very good energy resolution, perform a careful multilevel R-matrix analysis of the observed resonance structure to obtain the scattering functions for each of the first few partial waves and, finally, to average over energy to obtain the experimental OMP scattering functions for the individual partial waves. We previously followed that procedure for a dispersive OMP description of the n-^{86}Kr system [21].

Recently, a high-resolution measurement with a detailed R-matrix analysis was reported [22] for the total cross section of ^{40}Ar for neutron energies up to 1.5 MeV. The energy-averaged neutron total cross sections were included for higher energies up to 40 MeV. As we will show, those averaged total cross sections exhibit nearly the same anomaly for $0<E<10$ MeV as was found [10,11] for ^{40}Ca. It is of interest, therefore, to examine the empirical low-energy scattering functions for ^{40}Ar to see if they give evidence for a parity dependence of the imaginary potential. Unfortunately, a complete DOMA for n-^{40}Ar, similar to that [10] for n-^{40}Ca is not possible because there are insufficient data, i.e., there are no differential cross sections or analyzing powers, there are fewer bound states observed, the total cross sections only extend to 40 MeV rather than to 80 MeV as for ^{40}Ca, and the statistical uncertainties in those cross sections are relatively large. For this reason we will adapt the dispersive OMP from the n-^{40}Ca system [10] to n-^{40}Ar by adjusting two parameters of the model.

Our paper is organized as follows. In Sec. II we recall the form and the parameters of the dispersive OMP deduced from the DOMA [10] for n-^{40}Ca. (The VMA for n-^{40}Ca became available [11] after this work was completed.) In Sec. II C we adjust two model parameters to fit the Fermi energy E_F for the n-^{40}Ar system and the averaged neutron total cross sections for $11<E<40$ MeV. In Sec. III we compare the predictions of this model with the observed spacings of the bound states, with the s- and p-wave averaged scattering functions for $0<E<1.5$ MeV and with the neutron total cross section for $2<E<11$ MeV. In Sec. IV, we introduce a partity dependence into the surface imaginary potential to force excellent agreement with the s-wave and p-wave scattering functions and we find that this parity-dependent model significantly improves the fit to the total cross section for $2<E<11$ MeV. Section V is our discussion.

II. THE PARITY-INDEPENDENT MODEL

A. Formulation

We recall the form of the fixed-geometry, parity-independent dispersive OMP used [10] for the DOMA for n-^{40}Ca. The equations in Ref. [10] were written in terms of the neutron energy E but here we rewrite them in terms of the energy [20] relative to the Fermi energy:

$$\mathcal{E}=E-E_F \ . \tag{2.1}$$

The mean field is the sum

$$\mathcal{M}(r;\mathcal{E})=\mathcal{V}_H(r;\mathcal{E})+\Delta\mathcal{V}(r;\mathcal{E})+i\mathcal{W}(r;\mathcal{E}) \ , \tag{2.2}$$

where $\mathcal{V}_H(r;\mathcal{E})$ is the local equivalent to a Hartree-Fock-(HF-) type potential, $\mathcal{W}(r,\mathcal{E})$ is the imaginary com-

ponent, and $\Delta\mathcal{V}(r;\mathcal{E})$ is the dispersive contribution. The additional spin-orbit component is evaluated using empirical parameters from the literature (Eq. (3.1) of Ref. [10]).

For the energy region considered here, the central depth of the HF-type potential varies exponentially with energy:

$$\mathcal{V}_H(r;\mathcal{E})=V_H(0)e^{\alpha\mathcal{E}/V_H(0)}f(r;r_H;a_H)\ , \tag{2.3}$$

where $V_H(0)$ is the central depth at $\mathcal{E}=0$ and where r_H and a_H are energy-independent parameters for the radius and diffuseness for the Woods-Saxon form factor.

The imaginary field is the sum of a volume component, which has the same shape as the HF field, and a surface component, which is a Woods-Saxon derivative with energy-independent parameters r_s and a_s:

$$\mathcal{W}_v(r,\mathcal{E})=W_v(\mathcal{E})f(r;r_H;a_H)\ , \tag{2.4}$$

$$\mathcal{W}_s(r,\mathcal{E})=-4a_sW_s(\mathcal{E})\frac{d}{dr}f(r;r_s;a_s)\ . \tag{2.5}$$

The monotonic increase with energy for the volume depth is parametrized by the Brown-Rho [23] (BR) form and the rise and fall of the surface depth is parametrized as the difference between two BR forms:

$$W_v(\mathcal{E})=W_v^{\infty}\frac{\mathcal{E}^2}{\mathcal{E}^2+\mathcal{E}_v^2}\ , \tag{2.6}$$

$$W_s(\mathcal{E})=W_s^{\infty}\left[\frac{\mathcal{E}^2}{\mathcal{E}^2+\mathcal{E}_{s1}^2}-\frac{\mathcal{E}^2}{\mathcal{E}^2+\mathcal{E}_{s2}^2}\right]\ . \tag{2.7}$$

The five parameters in Eqs. (2.6) and (2.7) are correlated by the assumption that the volume integral for the full imaginary potential has a BR form such that the decrease of the surface component at high energies is compensated by the increase in the volume component. The number of free parameters is thereby reduced to three, say, the surface parameters, W_s^{∞}, $\mathcal{E}_{s1}$, and $\mathcal{E}_{s2}$, with the following relations for the other two:

$$\mathcal{E}_v=\mathcal{E}_{s2}\ , \tag{2.8}$$

$$G_vW_v^{\infty}=G_sW_s^{\infty}\ , \tag{2.9}$$

where G_v and G_s are the usual factors for converting well depths to volume integrals.

The dispersive well depths are calculated from the imaginary well depths using the dispersion relation

$$\Delta V_x(\mathcal{E})=\frac{\mathrm{P}}{\pi}\int_{-\infty}^{\infty}\frac{W_x(\mathcal{E}')d\mathcal{E}'}{\mathcal{E}'-\mathcal{E}}\ , \tag{2.10}$$

where P denotes the principal value integral and x denotes either surface or volume, s or v. These integrals are evaluated with the assumption that the central depths, $W_s(\mathcal{E})$ and $W_v(\mathcal{E})$, are each symmetric about the Fermi energy. The predicted dispersive terms have the same energy-independent shapes as do the corresponding imaginary parts.

B. Parametrization [10] for n-^{40}Ca

The Fermi energy E_F was taken to be midway between the ground-state energies for the two nuclei, ^{41}Ca and ^{39}Ca, which are formed by addition or subtraction of a neutron from ^{40}Ca. Thus, $E_F=-12$ MeV. The DOMA was performed [10] using the extensive set of data outlined in Sec. I to establish the values for the nine free parameters and the two correlated parameters:

$$r_H=1.18\text{ fm},\quad a_H=0.70\text{ fm}\ , \tag{2.11}$$

$$r_s=1.26\text{ fm},\quad a_s=0.60\text{ fm}\ , \tag{2.12}$$

$$W_s^{\infty}=-8.7\text{ MeV}\ ,$$

$$\mathcal{E}_{s1}=15\text{ MeV}\ , \tag{2.13}$$

$$\mathcal{E}_{s2}=130\text{ MeV}\ ,$$

$$W_v^{\infty}=-14.6\text{ MeV},\quad \mathcal{E}_v=\mathcal{E}_{s2}\ , \tag{2.14}$$

$$V_H^{\mathrm{Ca}}(0)=-58.8\ MeV,\quad \alpha^{\mathrm{Ca}}=0.55\ . \tag{2.15}$$

The superscript Ca for the HF depth parameters indicates that these will be changed for the following analysis of the n-^{40}Ar system.

In Fig. 1, the curve represents the total cross section for ^{40}Ca predicted by this model, and the points represent the observed cross sections for natural Ca. This figure is the same as Fig. 3 of Ref. [10] except that here it is plotted on an expanded energy scale to facilitate comparison with the corresponding figure given below for ^{40}Ar. A clear discrepancy is seen between model and experiment for $0<E<9.5$ MeV.

In Fig. 2, the two left-hand diagrams represent the predicted and observed bound-state structures for the n-^{40}Ca system. These diagrams are the same as in Fig. 12 of Ref. [10] except that here the $1d_{5/2}$ and $1f_{5/2}$ states are omitted because there are insufficient data for the corresponding states for n-^{40}Ar.

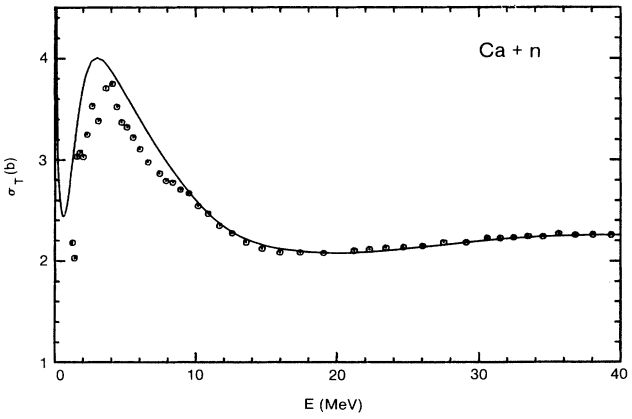

FIG. 1. Neutron total cross section for ^{40}Ca. Both the data points and the theoretical curve are replotted from Ref. [10]. The data are for natural calcium (97% ^{40}Ca) and the curve is calculated for ^{40}Ca from the dispersive optical model potential recalled here in Secs. II A and II B.

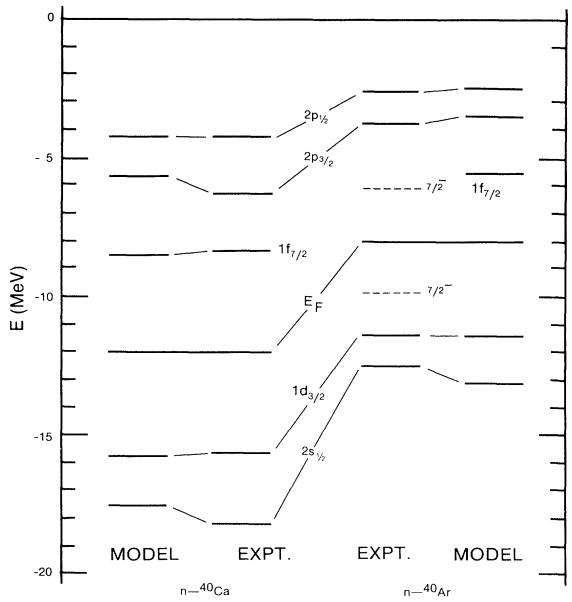

FIG. 2. Experimental and calculated energies for levels in the valence shells for the n-^{40}Ca and n-^{40}Ar systems. Energies from Table I are represented by the experimental structure for n-^{40}Ar. The dashed lines for the ground states for ^{41}Ar and ^{39}Ar indicate that these are not single-particle energies. The n-^{40}Ca structure is taken from Ref. [10] except that the $1f_{5/2}$ particle and $1d_{5/2}$ hole states are omitted here.

C. Parametrization for n-^{40}Ar

As stated in Sec. I, there are insufficient data for a full DOMA for the n-^{40}Ar system. The most serious deficiency is the absence of differential cross sections; such data are required to establish the shape parameters of the real and imaginary components of the potential and to separate the imaginary potential into its volume and surface components. All of the other observed quantities for both n-^{40}Ar and n-^{40}Ca are sensitive only to certain combinations of the shapes and strengths of the potentials. For example, if we were to take the real part of the mean field to have a Woods-Saxon from with depth V and radius r, then the data other than the angular distributions would establish only the quantity Vr^n, where n is approximately 2. In the DOMA [10] for n-^{40}Ca, the shape parameters were deduced primarily from the angular distributions for $10 < E < 40$ MeV and subsequently were assumed to be constant for the full range $-80 < E < 80$ MeV.

Although there are no angular distributions for ^{40}Ar, there are differential cross sections and analyzing powers for many other nuclei with $40 \leq A \leq 209$. Recent global OMP analyses [24,25] show that the shape of the mean field is nearly independent of target mass. We assume, therefore, that the shapes of each component of the mean field for n-^{40}Ar are the same as given by Eqs. (2.11) and (2.12) for n-^{40}Ca. Regarding the imaginary depths, we examine below the neutron total cross sections for ^{40}Ar for evidence that the imaginary volume integral is different than that for ^{40}Ca and, finding little difference, we keep the depths given by Eqs. (2.13) and (2.14) for ^{40}Ca.

With these assumptions, our model has only two free parameters, i.e., the HF depth parameters $V_H^{\rm Ar}(0)$ and $\alpha^{\rm Ar}$. We will deduce these from the empirical bound-state structure for the n-^{40}Ar system and from the energy-averaged neutron total cross sections. In Fig. 3 the symbols represent the neutron total cross sections [22] for ^{40}Ar and the vertical heights of the symbols represent the uncertainties from counting statistics. The original multitude of high-resolution data points have been replaced by averages over appropriate energy intervals in order to show fewer points with a relatively smooth variation with energy. Table I lists the binding energies and spectroscopic factors for the bound particle and hole states. The spectroscopic factors are sums over the observed fragments and the energies are averages weighted by the individual factors. These data are from the best detailed measurements [26,27] with good energy resolution and are consistent with earlier work [28].

The ^{40}Ar nucleus differs from ^{40}Ca in that a pair of protons in the $1d_{3/2}$ orbit is replaced by a pair of neutrons in the $1f_{7/2}$ orbit outside the 20-neutron closed shell. The ground states of ^{39}Ar and ^{41}Ar both have $J^\pi = \frac{7}{2}^-$. In Table I the ^{41}Ar ground state is denoted by $(f_{7/2})^2 + f_{7/2}$ to indicate that it is formed by addition of an $f_{7/2}$ neutron to the $(1f_{7/2})^2$ pair. In a like manner, the notation $(f_{7/2})^2 - f_{7/2}$ for the ^{39}Ar ground state indicates that it is formed by pickup of one of the paired neutrons. The 3.8-MeV energy difference shows that the pairing energy is large. Following the same procedure as for the n-^{40}Ca analysis, we place E_F midway between these ground states:

$$E_F = -8.0 \text{ MeV} \quad \text{for } n\text{-}^{40}\text{Ar} . \tag{2.16}$$

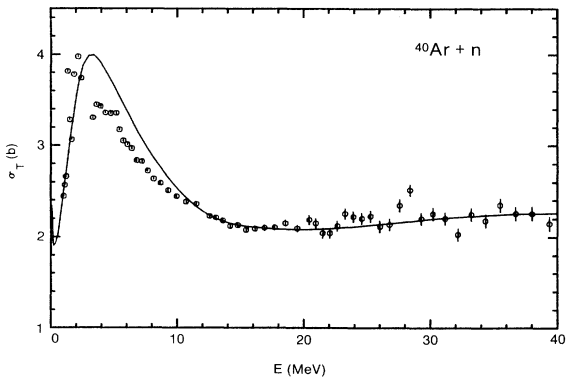

FIG. 3. Neutron total cross section for ^{40}Ar. The points represent energy-averaged experimental cross sections from Ref. [22] and the curve is the cross section calculated from the dispersive optical model potential from Sec. II C.

TABLE I. Experimental energies and spectroscopic factors of particle and hole states for n-^{40}Ar.

	Particle states[a]			Hole states[b]	
nlj	E (MeV)	$(2j+1)S_n^-$	nlj	E (MeV)	S_n^+
$(f_{7/2})^2+f_{7/2}$	−6.10	4.0	$(f_{7/2})^2-f_{7/2}$	−9.87	2.4
$2p_{3/2}$	−3.75	3.5	$1d_{3/2}$	−11.39	3.2
$2p_{1/2}$	−2.64	1.8	$2s_{1/2}$	−12.48	1.4

[a]From ^{40}Ar(d,p) stripping in Ref. [26].
[b]From ^{40}Ar(p,d) pickup in Ref. [27].

In Fig. 2, the n-^{40}Ar levels from Table I are represented by the second structure from the right. The ground states are shown by dashed lines, rather than sold, and are labeled $\frac{7}{2}^-$, rather than $1f_{7/2}$, to indicate that neither represents the true energy of the $1f_{7/2}$ orbit. The other levels are shown by solid lines and are labeled as single-particle or single-hole states; by this notation, we make the tacit assumption that the particle or hole states are reached by stripping or pickup without disturbing the paired $f_{7/2}$ neutrons in the ^{40}Ar core. We justify that approximation by the fact that the two $f_{7/2}$ particles have a large pairing energy.

A comparison of the two experimental structures in Fig. 2 shows that the binding energies are much less for n-^{40}Ar than for n-^{40}Ca. Clearly, the depth of the HF component must be less for n-^{40}Ar than for n-^{40}Ca. Essentially, two sets of data are required to determine the two HF parameters $V_H^{\rm Ar}(0)$ and $\alpha^{\rm Ar}$. For one set we take the energies from Table I for the $2p_{1/2}$, $2p_{3/2}$, $2s_{1/2}$, and $1d_{3/2}$ bound states. For the other we take the total cross sections for $11<E<40$ MeV from Fig. 3. (We omit the total cross sections for $E<11$ MeV because we want our procedure to be somewhat parallel to the DOMA [10] for n-^{40}Ca, for which the low-energy data carried little weight.) To first order, we adjust the depth $V_H^{\rm Ar}(0)$ to produce an average fit to the bound states and then choose the energy coefficient $\alpha^{\rm Ar}$ to give a good description of the total cross sections. Since the two parameters have some correlation, we iterate these steps to obtain the best overall fit. For the following discussion, we present figures based on our final parameters. These are

$$V_H^{\rm Ar}(0)=-53.2\pm0.5\ \text{MeV}\ , \tag{2.17}$$

$$\alpha^{\rm Ar}=0.39\pm0.05\ . \tag{2.18}$$

The curve of Fig. 3 represents the total cross section calculated from our model. For the fitted region, $11<E<40$ MeV, the curve agrees well with the average trend of the empirical points. In Fig. 2, the right-hand diagram represents the bound-state structure calculated from the real part of the model, i.e., from the HF plus dispersive components. The structure agrees well with that observed.

We estimated the uncertainly for $\alpha^{\rm Ar}$ in Eq. (2.18) by comparing the empirical cross sections for $11<E<40$ MeV in Fig. 3 to calculated curves for various values of $\alpha^{\rm Ar}$. We also investigated the effects of varying the coefficient W_s^∞ in Eq. (2.7) for the surface imaginary potential. In this we were motivated by the fact that the imaginary part of the symmetry potential is expected to reduce the surface depth for ^{40}Ar relative to ^{40}Ca. Actually, we found no evidence for this reduction. On the contrary, we found the fit to be slightly improved by an increase rather than a reduction of the depth. Following that study we assumed, as stated above, that the surface imaginary potential for ^{40}Ar is the same as for ^{40}Ca.

We now describe our method for adjusting $V_H^{\rm Ar}(0)$ and for estimating its uncertainty. The curves in Figs. 4(a) and 4(b), respectively, represent the depth W_s for the imaginary surface potential and the corresponding real dispersive depth ΔV_s. These are the same as deduced [10] from the DOMA for n-^{40}Ca, except that here they are shifted upward by 4 MeV in neutron energy because E_F is −8 MeV rather than −12 MeV. To illustrate our procedure, we calculate the level energies using our final HF depth from Eqs. (2.17) and (2.18). We temporarily ig-

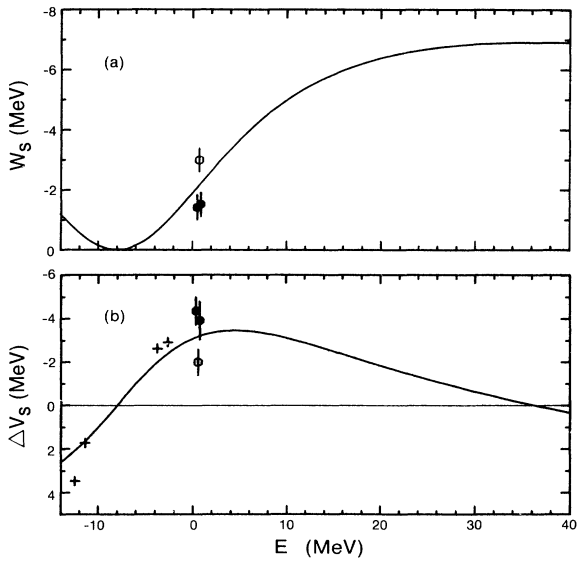

FIG. 4. (a) Imaginary and (b) real dispersive surface potentials for n-^{40}Ar. The curves are for the model in Sec. II C. In (b) the crosses represent the real dispersive depths required to bind the $2s_{1/2}$, $1d_{3/2}$, $2p_{1/2}$, and $2p_{3/2}$ states exactly at the empirical energies from Table I. The open (solid) points show the surface depths required to fit the energy-averaged s-wave (p-wave) scattering functions in the resonance region.

nore the dispersion constraint, Eq. (2.10), and adjust the surface depths to fit exactly the energies from Table I for the $(2s_{1/2}, 1d_{3/2})$ holes and $(2p_{3/2}, 2p_{1/2})$ particles. The adjusted surface depths are represented by the crosses in Fig. 4(b). The fact that the crosses for the particles and holes lie symmetrically about the curve demonstrates that our final value $V_H^{\rm Ar}(0)$ is well chosen. Equivalent agreement between the model and empirical level structures are seen in Fig. 2 for n-^{40}Ar; there the particle states for the model are slightly underbound, whereas the $1d_{3/2}$ hole is about right and the $2s_{1/2}$ hole is overbound. We investigated the sensitivity of the calculated structure to changes in $V_H^{\rm Ar}(0)$. If, for example, we had chosen $V_H^{\rm Ar}(0)$ to be 0.5 MeV deeper, the crosses in Fig. 4(b) for the particles would have moved down to the curve but those for the holes would have moved downward away from the curve. A decreased depth would have the opposite effect. Related shifts would appear in the structure of Fig. 2. From these studies we estimated the uncertainty in $V_H^{\rm Ar}(0)$ given in Eq. (2.17).

III. PREDICTIONS FROM THE MODEL

A. Particle-hole gap

Let us define a centroid E_c and particle-hole gap E_{ph} for the four bound states considered above:

$$E_c=[E(p_{1/2})+E(p_{3/2})+E(s_{1/2})+E(d_{3/2})]/4 , \quad (3.1)$$

$$E_{ph}=[E(p_{1/2})+E(p_{3/2})-E(s_{1/2})-E(d_{3/2})]/2 . \quad (3.2)$$

The empirical and model values for the centroid E_c are -7.57 and -7.62 MeV. This agreement merely demonstrates that the central depth $V_H^{\rm Ar}(0)$ at the Fermi energy is well chosen. The empirical and model particle-hole gaps are 8.74 and 9.33 MeV; the fact that these are in quite good agreement represents a successful prediction from the model because no parameter was adjusted to fit the empirical E_{ph}. The important role of the dispersive surface term for this prediction is demonstrated in Fig. 4(b) by the fact that the crosses closely follow the shape of the dispersive curve.

This prediction is also related to the HF effective mass, $m_H^*(r,\mathcal{E})$, which is defined by

$$m_H^*(r;\mathcal{E})/m=1-\frac{d}{dE}\mathcal{V}_H(r;\mathcal{E}) . \quad (3.3)$$

At the nuclear center and at the Fermi energy, one has

$$m_H^*(0;0)/m=1-\alpha . \quad (3.4)$$

To fit both the total cross sections and the bound-state centroid, we reduced the energy coefficient α from 0.55 for ^{40}Ca to 0.39 for ^{40}Ar. In other words, we increased the central effective mass from 0.45 for ^{40}Ca to 0.61 for ^{40}Ar. This decreases the predicted gap E_{ph}. If we were to return the coefficient α to 0.55, E_{ph} would be increased to 10.19 MeV, i.e., to 1.45 MeV larger than the empirical gap. Equivalently, the crosses in Fig. 4(b) would show a more rapid variation with energy than given by the dispersive curve.

B. Dispersive optical model in the resonance region

The primary motivation for the high-resolution measurements [22] of the neutron total cross section of ^{40}Ar was to resolve resonances at low energies. The R-matrix analysis [22] provides us with neutron-scattering functions for the $s_{1/2}$, $p_{1/2}$, and $p_{3/2}$ partial waves for the energy domain $E_l=0.0$ MeV to $E_u=1.5$ MeV. Here we compare the energy averages of those functions to the model predictions. A detailed discussion and justification of the following procedure is given in the section of Ref. [21] which deals with a similar analysis for ^{86}Kr.

In Ref. [22] for ^{40}Ar, the empirical scattering function $S_{lj}(E)$ for the neutron orbital angular momentum l and total angular momentum $j=l\pm\frac{1}{2}$ was parametrized in terms of a series of resonance energies and reduced widths, $E_{lj\lambda}$ and $\gamma^2_{lj\lambda}$, plus an external R function, $R_{lj}^{\rm ext}(E)$. In Fig. 5 the data points represent empirical values of $R_{lj}^{\rm ext}(E)$ obtained at six energies at which the resonance-potential interference patterns made it possible to deduce the small uncertainties which are represented by the vertical heights of the symbols. [The true $R_{lj}^{\rm ext}(E)$ must increase smoothly with increasing energy.] In Fig. 6, the "staircases" represent the cumulative sums of reduced widths up to the neutron energy E. Each riser is a reduced width, $\gamma^2_{lj\lambda}$, and each tread is the spacing between adjacent values of $E_{lj\lambda}$. The error bar at the top of each staircase corresponds to the fractional uncertainty, $(2/n)^{1/2}$, for a sum of n widths drawn at random from a Porter-Thomas distribution.

The complicated energy dependence of each $S_{lj}(E)$ must be averaged before comparison to the model. Good agreement between model and experiment requires that the model scattering function be approximately equal to the smoothed experimental average:

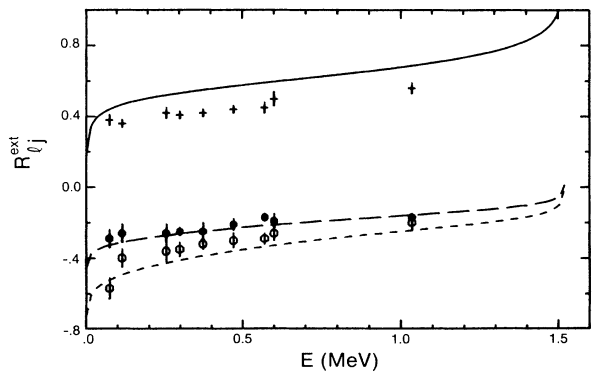

FIG. 5. Experimental and predicted external R functions in the resonance energy domain. Experimental values are plotted as crosses for $s_{1/2}$, circles for $p_{1/2}$, and points for $p_{3/2}$ partial waves. The vertical heights of the symbols are estimated uncertainties. The predicted curves are solid for $s_{1/2}$, short-dashed for $p_{1/2}$, and long-dashed for $p_{3/2}$ partial waves. Both predicted and experimental R-function expansions used a 5.0-fm channel radius.

$$S_{lj}^{\mathrm{OM}}(E)\cong\langle S_{lj}(E)\rangle \ . \tag{3.5}$$

Studies [29,30] with numerical averaging have shown this comparison can be accomplished by a simple prescription which has an analytic basis [29–31]. To utilize that prescription, we expand the model scattering function in terms of a smoothly varying complex R-function:

$$S_{lj}^{\mathrm{OM}}(E)=e^{-2i\phi_l(E)}\frac{1+iP_l(E)\mathcal{R}_{lj}^{\mathrm{OM}}(E)}{1-iP_l(E)\mathcal{R}_{lj}^{\mathrm{OM}}(E)} \ , \tag{3.6}$$

$$\mathcal{R}_{lj}^{\mathrm{OM}}(E)=R_{lj}^{\mathrm{OM}}(E)+i\pi s_{lj}^{\mathrm{OM}}(E) \ , \tag{3.7}$$

where $P_l(E)$ and $\phi_l(E)$ are the penetrability and the hard-sphere phase shift evaluated at the same channel radius as used for the empirical R function. We then use the following simple prescription for comparing the model functions to the averaged empirical functions:

$$R_{lj}^{\mathrm{ext}}(E)\cong R_{lj}^{\mathrm{OM}}(E)-\mathrm{P}\int_{E_l}^{E_u}\frac{s_{lj}^{\mathrm{OM}}(E')dE'}{E'-E} \ , \tag{3.8}$$

$$\sum_{\lambda=1}^{\lambda=k}\gamma_{lj\lambda}^2\cong\int_{E_l}^{E_k}s_{lj}^{\mathrm{OM}}(E')dE' \ , \tag{3.9}$$

where P denotes the principal value integral.

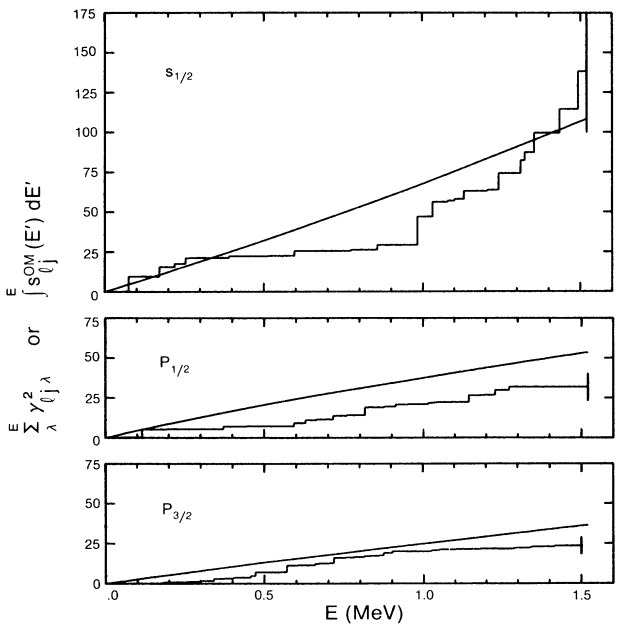

FIG. 6. Sums of experimental reduced neutron widths and integrals of predicted strength functions for the $s_{1/2}$, $p_{1/2}$, and $p_{3/2}$ neutron partial waves for ^{40}Ar in the resonance region. The heights of the risers for the "staircases" are reduced widths and the lengths of the treads are the spacings between adjacent levels. The error bars show the uncertainties in the full sums for assumed Porter-Thomas distributions of widths. The curves represent integrals up to the energy of E of the strength functions from the model. Both predicted and experimental R-function expansions used a 5.0-fm channel radius.

As described above, the empirical or left-hand sides of Eqs. (3.8) and (3.9) are plotted in Figs. 5 and 6, respectively. The model predictions for the right-hand sides of the equations are represented by the curves in those figures. In Fig. 5 the model predicts correctly that R^{ext} is much more positive for s waves than the p waves. That is because the $3s_{1/2}$ state is unbound such that it makes a positive contribution to R^{ext} whereas the $2p_{1/2}$ and $2p_{3/2}$ states are bound such that they contribute negatively. Also, in Fig. 6, the model predicts correctly that the $s_{1/2}$ strength function is relatively large; that is because the unbound $3s_{1/2}$ state is nearby. Finally, the model predicts correctly, by virtue of its spin-orbit component, that the strength function is larger and the R^{ext} more negative for $p_{1/2}$ that for $p_{3/2}$; that is, because the bound $2p_{1/2}$ state is closer to the resonance region than the more deeply bound $2p_{3/2}$ state.

To examine these predictions more closely and to study the roles of the imaginary and dispersive components, we follow a procedure similar to that described for the bound states in Sec. II C. We temporarily ignore the dispersion constraint and adjust the real and imaginary surface potentials for each partial wave to force very good agreement with the averaged scattering functions. Our criteria for $R_{lj}^{\mathrm{ext}}(E)$ is that the model function on the right-hand side Eq. (3.8) give the best least-squares fit to the points in Fig. 5. Our criteria for the sum of reduced widths is that, when the integral on the right-hand side of Eq. (3.9) is extended over the full domain, it agrees well with the empirical sum for the full domain. (We choose the full domain to minimize the uncertainty that is inherent in a small sample of reduced widths.) For p-waves, we can satisfy the two criteria by making independent adjustments in the real and imaginary surface potentials because there is little correlation in their effects on the real and imaginary parts of the complex R function. This lack of correlation is related to the fact that the single-particle $2p_{1/2}$ and $2p_{3/2}$ states lie well below the resonance domain. The same independence does not hold for $s_{1/2}$ waves because the $3s_{1/2}$ state is only slightly unbound. For that case we must adjust the real and imaginary surface potentials together to achieve the best overall fulfillment of the two criteria.

The resulting surface depths are represented at the center of the domain in Fig. 4 by a circle for s waves and by solid points for p waves. The heights of the symbols represent the uncertainties estimated from those shown in Figs. 5 and 6. We see that the model curves in both Figs. 4(a) and 4(b) pass about midway between the solid and open circles such that the empirical average for the two parities agrees well with the prediction. The agreement in Fig. 4(a) for the imaginary potential confirms that the strength of the potential decreases rapidly as the energy is reduced towards the Fermi energy, and the agreement in Fig. 4(b) supports the prediction that real dispersive term rises to near its maximum in the resonance region. The good agreement for the average over parities is related to the fact that the model curve and empirical cross sections in Fig. 3 agree well for $E<1.5$ MeV. In Sec. IV we examine the separate s- and p-wave values more closely.

C. Neutron total cross sections for $E < 11$ MeV

In Fig. 3 the predicted total cross sections for $2 < E < 11$ MeV show poor agreement with those observed. Figure 1 shows that a similar discrepancy was found for $E < 9.5$ MeV from the DOMA analysis for ^{40}Ca. Furthermore, the analysis [10] of the differential cross sections for ^{40}Ca for $E < 9.5$ MeV showed an anomalous behavior in that the empirical HF and dispersive potential depths deviated from the curves from the model. (See Figs. 4 and 5 of Ref. [10].)

IV. PARITY-DEPENDENT MODEL

Even though the averages for the empirical s-wave and p-wave values in Fig. 4 agree well with the model curves, the individual s-wave and p-wave symbols do deviate from the curves by more than the experimental uncertainties. We now examine the possibility that these small deviations result from a parity dependence in the imaginary potential and that the same parity dependence may account for the deviations in the total cross sections from the predictions for $2 < E < 11$ MeV.

Obviously, the circle and points for the imaginary potential in Fig. 4(a) could be fit at once by introducing a parity dependence such that the even-parity imaginary curves is raised up to go through the $s_{1/2}$ circle and the odd-parity curve is lowered to pass close to the $p_{1/2}$ and $p_{3/2}$ points. An infinity of curves could be drawn; however, the only ones allowed by the dispersive constraint are those for which the corresponding real dispersive curves pass through the points or circle in Fig. 4(b). The general shape imposed on the imaginary curve by the constraint can be understood from the dispersion integral, Eq. (2.10), by noting that the contributions from regions above and below an energy $\mathcal{E}$ contribute with opposite signs to the integral. For $s_{1/2}$ waves, both the requested increase in the imaginary depth and the decrease in the dispersive depth can be achieved if the imaginary curve rises slowly below the resonance region and decreases fairly rapidly above the region. The reverse holds for p waves.

Our procedure is to allow four free energy parameters to define the rise and fall of the even- and odd-parity imaginary depths. All other parameters are held fixed as given in Sec. II C. Then there are altogether three more parameters than for our original parity-independent model. For the even-parity depth we take the difference between two BR forms [23], as in Eq. (2.7), with rising and falling energy parameters, $\mathcal{E}_{e1}$ and $\mathcal{E}_{e2}$:

$$W_e(\mathcal{E}) = W_s^{\infty}\left[\frac{\mathcal{E}^2}{\mathcal{E}^2+\mathcal{E}_{e1}^2} - \frac{\mathcal{E}^2}{\mathcal{E}^2+\mathcal{E}_{e2}^2}\right] . \tag{4.1}$$

For the odd-parity depth, we define the rising and falling parameters $\mathcal{E}_{o1}$ and $\mathcal{E}_{o2}$. However, since we need a rapid rise, we replace the rising BR form by the more rapidly rising Jeukenne-Mahaux [32] form

$$W_0(\mathcal{E}) = W_s^{\infty}\left[\frac{\mathcal{E}^4}{\mathcal{E}^4+\mathcal{E}_{o1}^4} - \frac{\mathcal{E}^2}{\mathcal{E}^2+\mathcal{E}_{o2}^2}\right] . \tag{4.2}$$

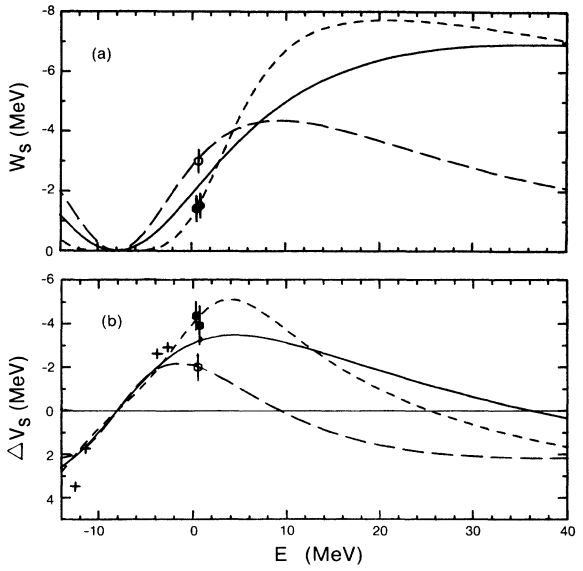

FIG. 7. (a) Parity-dependent imaginary and (b) real surface potentials. Depths for even and odd parities are represented by long- and short-dashed curves, respectively. The solid curve and the data points are from Fig. 4.

We adjust the four energy parameters, much as discussed in Sec. III B, to fit by least squares the R^{ext} points in Fig. 5 and the sums of reduced widths in Fig. 6. This yields

$$\mathcal{E}_{e1} = 10 \text{ MeV}, \quad \mathcal{E}_{e2} = 30 \text{ MeV} , \tag{4.3a}$$

$$\mathcal{E}_{o1} = 12.7 \text{ MeV}, \quad \mathcal{E}_{o2} = 100 \text{ MeV} . \tag{4.3b}$$

The corresponding well depths are represented in Figs. 7(a) and 7(b) by short-dashed and long-dashed curves for odd and even parities, respectively. Here the solid curves

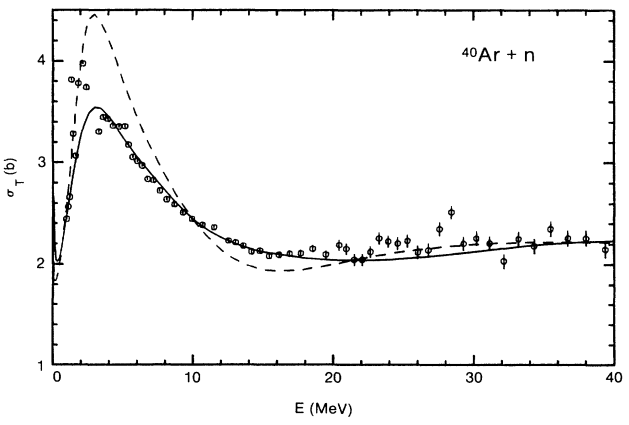

FIG. 8. Neutron total cross section for ^{40}Ar predicted from the model with parity-dependent imaginary surface potentials. The solid curve is predicted from the parity-dependent model of Sec. IV and the dashed curve is for a model with the parities reversed for the real and imaginary curves in Fig. 7. The data points are the same as in Fig. 3.

and the data points are reproduced from Fig. 4. We see that the solid and open points agree well with the odd and even curves, respectively. This is as expected because, essentially, we have used four free parameters to fit four empirical data. Also, the new dashed curves maintain agreement with the bound-state symbols for the $2s_{1/2}$, $2p_{1/2}$, and $2p_{3/2}$ levels.

The somewhat surprising result is that this parity-dependent model, which has been parametrized from data only for the energy region $0 < E < 1.5$ MeV, gives a much improved prediction to the total cross section for $2 < E < 11$ MeV. This improvement is demonstrated in Fig. 8, where the points are reproduced from Fig. 3 and the solid curve represents the total cross section predicted from the new model. One might suspect that the improvement results from an average change for the various partial waves, rather than from a specific parity dependence. To address this question, we reversed the parities of the two imaginary curves (also the dispersive curves) and repeated the calculations of total cross sections. The resulting prediction is represented by the dashed curve in Fig. 8; it gives a poor fit to the data. We tried other combinations of partial waves and concluded that the assumption of a parity dependence is most reasonable.

V. DISCUSSION

The fixed-geometry, l-independent, dispersive optical model potential which was previously developed [10] for the n-^{40}Ca system from extensive data for a broad neutron energy region was modified here to describe a limited set of data for the n-^{40}Ar system. The Fermi energy E_F was taken to be -8 MeV and the parametrization was done by adjusting only the depth of the Hartree-Fock component while keeping all other parameters the same as for n-^{40}Ca. Essentially, this parametrization was accomplished in two steps: firstly, the central depth of the HF potential at E_F was adjusted to achieve a good fit to the centroid of the bound particle and hole states of the valence shells and, secondly, the energy coefficient for the depth was adjusted to fit the neutron total cross sections for $11 < E < 40$ MeV.

The resulting central HF potential for n-^{40}Ar is -53.2 MeV at the system's Fermi energy, $E_F = -8$ MeV. This is compared to -58.8 MeV for n-^{40}Ca at its Fermi energy, $E_F = -12$ MeV. The energy coefficient for n-^{40}Ar is 0.39; it was 0.55 for n-^{40}Ca. Qualitatively, both changes were expected from the influence of the symmetry potential. The ^{40}Ar nucleus has an excess of neutrons relative to ^{40}Ca and the symmetry potential takes care of the fact that the n-n interaction is weaker than the n-p interaction. Also, the energy coefficient decreases for ^{40}Ar because the symmetry potential decreases with increasing energy [33].

As discussed in Sec. III A, the good description achieved in Fig. 2 for the bound-state spectrum demonstrates the need for the dispersive terms. It also demonstrates the need for the reduced HF energy coefficient or equivalently, for an increased central effective mass such that the predicted energy spectrum is adequately "compressed" relative to the n-^{40}Ca spectrum.

In Sec. III B, we compared empirical [22] energy-averaged s-wave and p-wave scattering functions for $E < 1.5$ MeV to predictions from the model. Several trends in the empirical functions are correctly predicted. The comparison confirms that the surface imaginary potential is much shallower for $E < 1.5$ MeV than it is at several MeV and shows, as predicted by the dispersion relation, that the real surface dispersive term has nearly its maximum depth in the low-energy resonance region.

In Sec. III C we found that the only clear inadequacy in the model is that it predicts too high neutron total cross sections for $2 < E < 11$ MeV, as shown in Fig. 3. A similar failure for the original model [10] for n-^{40}Ca is seen in Fig. 1 for $1 < E < 9.5$ MeV. For the case of n-^{40}Ca, a search [10] of parameter space revealed no way to fit this region using the fixed-geometry, l-independent model.

In Sec. IV, we investigated this discrepancy in total cross sections for n-^{40}Ar in relation to the data in the resonance region. We noted that, even though the empirical s-wave and p-wave scattering functions for $0 < E < 1.5$ MeV agree on the average with the predictions from the model, there is a hint of parity dependence. We then found that the introduction of a parity dependence into the imaginary potential to fit the individual s-wave and p-wave scattering functions substantially reduces the discrepancy in total cross section for $2 < E < 11$ MeV.

There are at least two reasons for caution regarding the proposed parity dependence. One is that it comes from empirical scattering functions that have fairly large uncertainties. Another is that, even if the averaged scattering functions were known precisely, it may be unreasonable to require the mean field to describe such details. On the other hand, the fact that the total cross sections for both ^{40}Ar and ^{40}Ca show very similar discrepancies from the predictions of the parity-independent model suggests that the phenomena might be described by a mean field. A related curious fact is that the divergences of the total cross sections from the model curves in Figs. 1 and 3 for ^{40}Ar and ^{40}Ca occur at different neutron energies near 10 MeV but at nearly identical energies relative to the average for the bound $2p_{1/2}$ and $2p_{3/2}$ states for the two systems. In this connection it has been pointed out recently [11] that the $p_{1/2}$ and $p_{3/2}$ imaginary components should go to zero at the binding energies for the $2p_{1/2}$ and $2p_{3/2}$ states.

In any case, if the surface real and imaginary components of the mean field do depend on orbital angular momentum in the resonance region, then the integral nature of the dispersive constraint requires that the effects be experienced over a rather broad region. It is a consequence of the constraint that our fitting in the resonance region $0 < E < 1.5$ MeV, makes a significant change in the total cross section all the way to about 10 MeV.

Of course, more data and analysis are desired, not only for this mass region but for other nuclei. New high-resolution resonance measurements with R-matrix analysis for neutrons on ^{40}Ca would be of particular interest. If a parity dependence were indicated, it would be incorporated into a new DOMA for the n-^{40}Ca system, for which there are much more data than for n-^{40}Ar.

Studies in the region of the 126-neutron shell continue to be of interest. The detailed analysis [19] for n-^{208}Pb that followed the original DOMA [12] led to the conclusion that the surface imaginary depth has an l dependence, similar to a parity dependence, and that the diffuseness decreases slowly below 10 MeV. It has been suggested [16] in connection with the DOMA for n-^{209}Bi that the apparent need for an l dependence for n-^{208}Pb might be removed if an improved form for the energy dependence for the imaginary strength were used; however, the use of an improved form for the variational moment approach [13] for n-^{208}Pb did not remove that need. In fact, both n-^{208}Pb and n-^{209}Bi may need an l dependence because the dispersive potentials required experimentally for $0 < E < 10$ MeV generally fall below the predicted dispersive curves for both systems. In the case of n-^{208}Pb, high-resolution resonance data and analyses should help. Such data and analyses were published [34] independently of the DOMA [12]; extensive new data are now available [35].

Studies have also been made for the 50-neutron shell. The nuclei ^{86}Kr, ^{89}Y, and ^{90}Zr each have 50 neutrons. An extensive DOMA [15] for n-^{90}Zr revealed little evidence for a low-energy anomaly; the predicted total cross section was too high at low energies, but only below about 3 MeV. A more limited n-^{86}Kr analysis [21], which parallels the present n-^{40}Ar analysis, showed no evidence of a parity dependence and little problems with the total cross section. On the other hand, the n-^{89}Y analysis [4] showed a low-energy behavior which suggests [20] a parity or state dependence.

There is active theoretical interest in a parity dependence. For example, a recent inversion analysis [36] of the empirical phase shifts for nucleon-^{4}He scattering showed a parity dependence in the real potential. Another recent paper [37] is devoted to the angular momentum dependence resulting from antisymmetrization for the nucleus-nucleus potential. It is well known [38,39] that, in principle, the imaginary optical potential is nonlocal, and microscopic calculations [40] using the nuclear structure approach [41] specifically for 30-meV neutrons on ^{40}Ca produced an imaginary potential with an angular-momentum dependence closely related to the spatial nonlocality. Those calculations gave well depths that varied [40] somewhat erratically with increasing l values, in qualitative agreement with the empirical grouping of l values found from the DOMA [12] for n-^{208}Pb. There is very little theoretical guidance for a detailed dependence of the imaginary potential at low energies. Reference [19] includes a qualitative discussion of the possible origin of the l dependence in relation to the n-^{208}Pb system. As stated above, the surface imaginary well depth $W_{slj}(\mathcal{E})$ is expected [11] to have a different threshold for each lj, depending on the position of the corresponding bound single-particle states. In the case of the n-^{208}Pb, system, there is empirical evidence [20] that quasibound states should be grouped with the bound states. For the lower partial waves, the resulting state dependence is approximately a parity dependence.

We are grateful to Prof. C. Mahaux and Dr. J. B. McGrory and Dr. G. R. Satchler for stimulating comments and discussions.

*Mailing address: Box 310, Rt. 1; Ten Mile, TN 37880.

[1] Su Zong Di and P. E. Hodgson, J. Phys. G **14**, 1485 (1988), and references cited therein.
[2] A. B. Smith, P. E. Guenther, and R. D. Lawson, Nucl. Phys. **A483**, 50 (1988), and references cited therein.
[3] P. A. Moldauer, Nucl. Phys. **47**, 65 (1965).
[4] R. D. Lawson, P. T. Guenther, and A. B. Smith, Phys. Rev. C **34**, 1599 (1986).
[5] R. D. Lawson, P. T. Guenther, and A. B. Smith, Phys. Rev. C **36**, 1298 (1987).
[6] R. D. Lawson, P. T. Guenther, and A. B. Smith, Nucl. Phys. **A493**, 267 (1989).
[7] J. R. M. Annand, R. W. Finlay, and F. E. Dietrich, Nucl. Phys. **A443**, 249 (1985).
[8] C. Mahaux and H. Ngô, Nucl. Phys. **A378**, 205 (1982).
[9] C. Mahaux and R. Sartor, in *Advances in Nuclear Physics*, edited by J. W. Negele and E. Vogt (Plenum, New York, 1991), Vol. 20, p. 1.
[10] C. H. Johnson and C. Mahaux, Phys. Rev. C **38**, 2589 (1988).
[11] C. Mahaux and R. Sartor, Nucl. Phys. (to be published).
[12] C. H. Johnson, D. J. Horen, and C. Mahaux, Phys. Rev. C **36**, 2252 (1987).
[13] C. Mahaux and R. Sartor, Nucl. Phys. **A493**, 157 (1989).
[14] W. Tornow, Z. P. Chen, and J. P. Delaroche, Phys. Rev. C **42**, 693 (1990).
[15] J. P. Delaroche, Y. Wang, and J. Rapaport, Phys. Rev. C **39**, 391 (1989).
[16] R. K. Das and R. W. Finlay, Phys. Rev. C **42**, 1013 (1990).
[17] C. Mahaux and R. Sartor, Nucl. Phys. **A503**, 525 (1989).
[18] C. Mahaux and R. Sartor, Phys. Rev. C **36**, 1777 (1987).
[19] J.-P. Jeukenne, C. H. Johnson, and C. Mahaux, Phys. Rev. C **38**, 2573 (1988).
[20] C. H. Johnson and R. R. Winters, Phys. Rev. C **37**, 2340 (1988).
[21] C. H. Johnson, R. F. Carlton, and R. R. Winters, Phys. Rev. C **39**, 415 (1989).
[22] R. R. Winters, R. F. Carlton, C. H. Johnson, N. W. Hill, and M. R. Lacerna, Phys. Rev. C **43**, 492 (1991).
[23] G. E. Brown and M. Rho, Nucl. Phys. **A372**, 397 (1981).
[24] R. L. Varner, T. B. Clegg, T. L. McAbee, and W. J. Thompson, Phys. Lett. B **185**, 6 (1987).
[25] R. L. Varner, W. J. Thompson, T. L. McAbee, E. J. Ludwig, and T. B. Clegg, Phys. Rep. **201**, 57 (1991).
[26] S. Sen, S. E. Darden, W. A. Yoh, and E. D. Berners, Nucl. Phys. **A250**, 45 (1975).
[27] J. F. Tonn, R. E. Segel, J. A. Nolen, W. S. Chien, and P. T. Debevec, Phys. Rev. C **16**, 1357 (1977).
[28] P. M. Endt and C. Van der Leun, Nucl. Phys. **A310**, 1 (1978).
[29] C. H. Johnson, N. M. Larson, C. Mahaux, and R. R. Winters, Phys. Rev. C **27**, 1913 (1983).
[30] C. H. Johnson, C. Mahaux, and R. R. Winters, Phys. Rev. C **32**, 359 (1985).
[31] A. M. Lane and R. G. Thomas, Rev. Mod. Phys. **30**, 257 (1958).

[32] J.-P. Jeukenne and C. Mahaux, Nucl. Phys. **A394**, 445 (1983).
[33] C. Mahaux and R. Sartor, Nucl. Phys. **A481**, 407 (1988).
[34] D. J. Horen, C. H. Johnson, J. L. Fowler, A. D. MacKellar, and B. Castel, Phys. Rev. C **34**, 429 (1986).
[35] R. F. Carlton, R. R. Winters, J. A. Harvey, N. W. Hill, C. H. Johnson, and J. Schmiedmayer, Bull. Am. Phys. Soc. **36**, 1349 (1991).
[36] S. G. Cooper and R. S. Mackintosh, Phys. Rev. C **43**, 1001 (1991).
[37] S. Yamaguchi, Phys. Rev. C **43**, 285 (1991).
[38] C. L. Rao, M. Reeves, III, and G. R. Satchler, Nucl. Phys. **A207**, 182 (1973).
[39] N. Vinh Mau and A. Bouyssy, Nucl. Phys. **A257**, 189 (1976).
[40] V. A. Madsen and F. Osterfeld, Phys. Rev. C **39**, 1215 (1989).
[41] F. Osterfeld, J. Wambach, and V. A. Madsen, Phys. Rev. C **23**, 179 (1981).